

Self-assembled Behaviors of Desulphurized MoS₂ Monolayer Sheets

Pinqiang Cao,^{1, 2, *} Jianyang Wu,^{2, *}

¹ School of Resources and Environmental Engineering, Wuhan University of Science and Technology,
Wuhan 430081, PR China

² Department of Physics, Research Institute for Biomimetics and Soft Matter, Jiujiang Research Institute,
Fujian Provincial Key Laboratory for Soft Functional Materials Research, Xiamen University, Xiamen
361005, PR China

Email address:

Pinqiang Cao: pinqiang@wust.edu.cn;

Jianyang Wu: jianyang@xmu.edu.cn;

*To whom correspondence should be addressed: pinqiang@wust.edu.cn; jianyang@xmu.edu.cn

Abstract: Self-assembled topological structures of post-processed two-dimensional materials exhibit novel physical properties distinct from those of their parent materials. Herein, the critical role of desulphurization on self-assembled topological morphologies of molybdenum disulfide (MoS_2) monolayer sheets is explored using molecular dynamics (MD) simulations. MD results show that there are differences in atomic energetics of MoS_2 monolayer sheets with different desulphurization contents. Both free-standing and substrate-hosted MoS_2 monolayer sheets show diversity in topological structures such as flat surface, wrinkles, folds and scrolls, depending on the desulphurization contents, planar dimensions and ratios of length-to-width of MoS_2 monolayer sheets. Particularly, at the critical desulphurization contents, they roll up into nanotube morphology, consistent with previous experimental observations. Moreover, the observed differences in the molecular morphological diagrams between free-standing and substrate-hosted MoS_2 monolayer sheets can be attributed to unique interatomic interactions and van der Waals interactions in them. The study provides important insights into functionalizing structural morphological properties of two-dimensional materials, *e.g.*, MoS_2 , via defect engineering.

Key Words: Molybdenum Disulfide; Desulphurization; Self-assemble; Structural Morphology

1 Introduction

Monolayer two-dimensional (2D) transition metal dichalcogenides (TMDs) structures have attracted significant attention as promising materials due to their important practical applications in the fields of electronic devices, energy storage, biosensors, bioimaging technologies, and catalysis [1-6](#). Particularly, among the TMDs' family, molybdenum disulfide (MoS_2) has attracted great attention because of its unique crystal structures and distinctive excellent physical properties, *e.g.*, electrical, optical, and mechanical properties.

To date, there are three most commonly encountered crystalline polymorphs of MoS_2 structures, namely, 1T, 2H, and 3R, where the letters stand for trigonal, hexagonal and rhombohedral structure, respectively, and the digit numbers indicate the layer number in the basic unit cell of MoS_2 structures [6,7](#). For each layer of the three polymorphs of MoS_2 , it is structurally characterized by S-Mo-S sandwiched structures and each transition molybdenum (Mo) atom is covalently bonded to six sulfur (S) atoms. For bulk structures, S-Mo-S layers are connected together by weak interlayer van der Waals (vdW) interactions [8](#). Importantly, molybdenum disulfide as a natural mineral is naturally abundant on Earth [9,10](#), and it is predominantly available in the 2H phase with trigonal prismatic coordination of Mo atoms. Synthetic MoS_2 may occur in the 3R phase and 1T phase as lithium intercalation is introduced [11](#). Critically, due to its unique structure, MoS_2 shows unique transport, electronic and mechanical properties. For example, monocrystalline MoS_2 monolayer exhibits a larger intrinsic direct bandgap of 1.8 eV than that of its bulk and other 2D material counterparts [9,12,13](#). Moreover, the mobility of a room-temperature MoS_2 monolayer was demonstrated to have at least $200 \text{ cm}^2 \cdot \text{V}^{-1} \cdot \text{s}^{-1}$, and transistors with a current on/off ratio exceeding 1×10^8 at room-temperature can be achieved [10](#). Mechanically, monolayer MoS_2 shows high Young's modulus and high flexibility [14-18](#). Interestingly, structural transformations between different crystal structures of MoS_2 have been observed [19-23](#).

Remarkably, topological defects such as vacancies, dislocations, and grain boundaries (GBs) in MoS₂ monolayer sheets play an important role in tuning their transport, electronic and mechanical properties [24-27](#). In reality, as a result of extra-large ratios of surface-to-bulk in monolayer MoS₂, topological defects are easily tended to be generated [28](#). For example, sulfur vacancies, hereafter also called as desulphurization in this work, in the basal plane of MoS₂ is one common type of topological defects. Such desulphurization induced topological defects can be introduced by ion sputtering and sulfur annealing [25, 29, 30](#). The introduction of sulfur vacancies can enhance hydrogen evolution reaction activity of monolayer MoS₂ [25, 31-34](#). In terms of magnetism [35](#), anion and cation vacancies and vacancy clusters in MoS₂ can result in ferromagnetic effects. In view of these interesting phenomena, it suggests that material performances of molybdenum disulfide can be modulated via topological defect engineering.

As a result of its large out-of-plane flexibility, 2D layered MoS₂ shows different surface morphologies at various external conditions [29, 36](#). For example, when a pre-stretched strain in the elastomeric substrate is suddenly released, well-aligned wrinkles of layered MoS₂ sheets can form as a consequence of buckling-induced delamination [37, 38](#). During mechanical exfoliation of MoS₂ sheets, few layer MoS₂ flakes spontaneously form wrinkles and are buckling-delaminated on elastomer substrates due to large elastic mismatch. Monolayer MoS₂ can form wrinkles under uniaxial mechanical loadings [39](#), which is also observed in graphene, h-boron nitride (h-BN), and black phosphorus (BP) [18, 40-42](#). Individual wrinkles in few-layer MoS₂ sheets were also observed as they are lithiated or mechanically processed, and these individual wrinkles are analogous to line dislocations in bulk materials, but they showed drastically different interaction behaviors. Intrinsic ripples in other 2D materials like graphene spontaneously appear due to thermal fluctuations [31, 35](#). Also, it was identified that S vacancies can lead to the formations of wrinkles of 2H MoS₂ [29](#). Despite a number of important findings focusing on the surface morphology of MoS₂ sheets have been reported, yet how the desulphurization affects the structural morphology of MoS₂ sheets remains unclear at molecular scale, particularly for the structural morphology phase versus

desulphurization contents. In this work, a series of molecular dynamics (MD) simulations are systematically performed to reveal the critical role of desulphurization on the structural morphology of monocrystalline MoS₂ monolayer sheets.

2 Methods

2.1 Molecular Models

Monocrystalline MoS₂ monolayer samples are generated to investigate desulphurization-induced changes in structural morphology of MoS₂. Unlike other 2D materials, *e.g.*, flat graphene, puckered honeycomb BP, MoS₂ possesses a S-Mo-S sandwiched structure. The unit cell of MoS₂ is composed of one molybdenum atom plus six sulfur atoms. Six S atoms form triangular prism with a Mo atom located in the center, then Mo and S atoms covalently share electrons. Contrarily, the different layers of S-Mo-S are weakly connected to each other through vdW interactions in the bulk MoS₂. The thickness of monolayer MoS₂ is approximately 0.65 nm¹⁰. Figures 1a and 1b show different viewed snapshots of monolayer and bilayer MoS₂ structures, where Mo and S atoms are red- and yellow-colored, respectively. Figures 1c and 1d show perspective snapshots of free-standing MoS₂ monolayer sheets and substrate-hosted MoS₂ monolayer sheets on large-area MoS₂ monolayer sheets with an in-plane dimension of 10 × 10 nm², respectively. Figure 1e shows a perspective snapshot of zoomed-in MoS₂ bilayers. To investigate the effect of S vacancies on the structural morphology of MoS₂ layers, desulphurization contents from 0.0-100% on one planar surface of MoS₂ samples with dimensions varying from 10 × 10 – 50 × 50 nm² and length-to-width ratios from 1:1 to 5:1 are considered for both free-standing and substrate-hosted MoS₂ monolayer sheets, respectively. All S vacancies (desulphurization) are generated on one surface of MoS₂ monolayer sheets by randomly deleting the S atoms on the one surface of MoS₂ monolayer. For clarity, the one surface of MoS₂ containing S vacancies is hereafter also called as top-surface of MoS₂ monolayer,

and the other one surface of MoS₂ without containing S vacancies is hereafter also called as bottom-surface of MoS₂ monolayer.

2.2 Forcefields of MoS₂ Structures

A many-body reactive empirical bond order (REBO)-type Mo-S potential developed by Liang *et al.*^{43, 44} is employed to describe the interatomic interactions in MoS₂ systems. The forcefield contains a many-body REBO potential⁴⁵ that describes the short-range interactions and a two-body Lennard-Jones potential for the long-range vdW interactions. It is capable of capturing Mo-S covalent bond breaking and reforming during molecular dynamics calculations. Furthermore, this potential has successfully been utilized to investigate physical and chemical properties of MoS₂ nanostructures^{23, 46-53}. Importantly, it also shows good description in the structure behaviors of MoS₂ and dealing with the point defects in MoS₂ samples^{52, 54}. The short-ranged interatomic interactions of Mo-S systems by REBO-type Mo-S forcefield are expressed as:

$$E_b = \frac{1}{2} \sum_i \sum_{j(>i)} [V^R(r_{ij}) - b_{ij}V^A(r_{ij})] \quad (1)$$

$$V^R(r) = f^C(r)(1 + Q/r)Ae^{-\alpha r} \quad (2)$$

$$V^A(r) = f^C(r) \sum_{n=1}^3 B_n e^{-\beta_n r} \quad (3)$$

where E_b is the total binding energy. $V^R(r_{ij})$ and $V^A(r_{ij})$ are a repulsive and an attractive reaction, respectively. r_{ij} is the distance between atoms i and j . The cutoff function $f^C(r)$ is obtained from the switching cutoff scheme. The values of parameters used in our MD simulations can be found in elsewhere^{43, 44}. The long-ranged vdW interactions in MoS₂ system are described by the 12-6 Lennard-Jones potential as:

$$E_{LJ}(r) = 4\epsilon \left[\left(\frac{\sigma}{r} \right)^{12} - \left(\frac{\sigma}{r} \right)^6 \right] \quad (4)$$

where r is the interatomic distance. σ and ϵ is chosen as 3.13Å and 0.00693 eV in this study, respectively.

2.3 MD Simulations

All the MD calculations are carried out using the Large-scale Atomic-Molecular Massively Parallel Simulator (LAMMPS) software package [55](#). At the beginning, all samples are quasi-statically relaxed to a configuration with local minimum energy through conjugate gradient method, with an energy tolerance of 1.0×10^{-4} eV and a force tolerance of 1.0×10^{-4} eV/Å, respectively. Then, MD relaxations are conducted with 1.0×10^6 timesteps at 298.15 K under the NVT (constant number of particles, constant volume, and constant temperature) ensemble. The Nosé-Hoover thermostat method with damping times of 0.1 ps is assigned to control the temperature. The velocity-Verlet integration algorithm is utilized to integrate the equations with a timestep of 1 fs in all MD simulations. Periodic boundary conditions (PBCs) are applied in all three orthogonal directions. Initial velocities of all Mo and S atoms in the MoS₂ samples are assigned following the Gaussian distribution at the given temperature. The thickness of monolayer MoS₂ is taken as 0.65 nm to express atomic stress [10](#). Based on the virial definition of stress, the atomic stress is computed using the forces on the atoms collected during the MD calculations. Both potential energy and atomic stress in our samples are averaged over 1000 timesteps to eliminate the fast fluctuations.

3 Results and Discussion

3.1 Energetics in Desulphurized MoS₂ Sheets

Figures 2a-2c show variations in the instantaneous atomic potential energy per atom of free-standing desulphurized MoS₂ monolayer sheets of 10×10 nm² with MD relaxation time varying from 0.0-1.0 ns. It should be noted that random sulfur defects occur on the top-surface of MoS₂ monolayer sheets. As a

result of S-Mo-S sandwiched structures, surface S atoms including bottom- and top-S atoms in MoS₂ monolayer sheets with different desulphurization contents show higher potential energy than interior Mo atoms. As the desulphurization content on the top-surface of MoS₂ monolayer sheets varies from 0.0-100%, there are significant changes in the instantaneous atomic potential energy per atom. As shown in Figure 2a, the instantaneous atomic potential energy per Mo atom rapidly converges to constant values with increasing relaxation time, indicating the stability of interior Mo atoms. Interestingly, the converged values of Mo atoms are monotonically increased with the increasing desulphurization content, suggesting that the stability of interior Mo atoms can be adjusted by desulphurization contents. As for both top- and bottom-S atoms (Figures 2b and 2c), however, it is identified that complex changes in the instantaneous atomic potential energy per S atom can occur. For example, there are fluctuations in the instantaneous atomic potential energy per S atom with the increasing relaxation time, although the instantaneous atomic potential energy per S atom tends to reach a constant value, suggesting complex changes in the structural morphology of MoS₂ monolayer sheets. Interestingly, when the desulphurization content on the top-surface of MoS₂ monolayer sheets changes from 0.0-100%, free-standing MoS₂ monolayer sheets show a transition behavior in the instantaneous potential energy per bottom-S atom (Figure 2b): Below desulphurization of 50%, the instantaneous atomic potential energy per bottom-S atom is increased with increasing desulphurization contents, whereas above which, it shows a reduction trend with increasing desulphurization contents. With regard to the case of top surface of free-standing desulphurized MoS₂ monolayer sheets, there is negligible difference in the instantaneous atomic potential energy per top-S atom for MoS₂ monolayer sheets with desulphurization of 0.0-30%, whereas above 40% desulphurization, the instantaneous atomic potential energy per top-S atoms is decreased with the increasing desulphurization. It should be noted that free-standing desulphurized MoS₂ monolayer sheets with planar dimensions varying from 20 × 20 to 50 × 50 nm² and length-to-width ratios from 2:1 to 5:1 show similar variations in the instantaneous atomic potential energy per atom with changing desulphurization contents (Figures S2-S4, and S7-S9). The instantaneous radius of gyration (R_g) is an appropriate way to

quantitatively measure the structural compactness and morphology. Figure 2d presents the variations in the instantaneous radius of gyration (R_g) with MD relaxation simulation time. As is seen, the R_g of desulphurized MoS₂ monolayer quickly converges to averaged values, and it varies from around 31-43 Å depending on the desulphurization contents. The free-standing MoS₂ monolayer sheets with less desulphurization show large values of R_g . Such changes in the R_g of free-standing desulphurized MoS₂ monolayer sheets indicate their distinct structural morphology. Particularly, the perfect sawtooth-like fluctuations in the R_g of MoS₂ sheets at the desulphurization content of 50% suggest the cyclic changes of structural morphology. Similar changes in the instantaneous radius of gyration with changing desulphurization contents are also observed in the other free-standing desulphurized MoS₂ monolayer sheets with dimensions varying from 20×20 to 50×50 nm² and length-to-width ratios from 2:1 to 5:1 (Figures S5 and S10).

Figures 3a-3c show the instantaneous atomic potential energy per atom of finite substrate-hosted desulphurized MoS₂ sheets of 10×10 nm² on large-area MoS₂ monolayer substrate as a function of MD simulation time. Apparently, there are differences in developments of the instantaneous atomic potential energy per atom of finite substrate-hosted desulphurized MoS₂ monolayer sheets under different desulphurization contents. Upon interior Mo atoms, the instantaneous atomic potential energy per molybdenum atom in finite substrate-hosted desulphurized MoS₂ monolayer sheets is initially increased with increasing relaxation time (Figure 3a). As the relaxation time reaches a critical value, however, it is reduced except for substrate-hosted desulphurized MoS₂ monolayer sheets with both desulphurization of 40% and 100%. With further relaxations, substrate-hosted MoS₂ monolayer sheets with desulphurization contents varying from 0-30% show constant values of the instantaneous atomic potential energy per Mo atom, indicating achievement of stable configurations. For the case of other desulphurization contents ranging from 40-100%, the instantaneous atomic potential energy per Mo atom is either continuously increased or decreased, relying on the desulphurization contents, indicative of metastable configurations.

As shown in Figure 3b and 3c, finite substrate-hosted desulphurized MoS₂ monolayer sheets with desulphurization of 0-30% shows convergence of instantaneous potential energy per surface top- or bottom-S atom, again suggesting their stable structural configurations, whereas that with desulphurization of 40-100% show monotonic decreases in the instantaneous atomic potential energy per surface top- or bottom-S atom, also indicating their metastable structures. The developments of the instantaneous atomic potential energy per atom of substrate-hosted MoS₂ monolayer sheets differ from that of free-standing ones, indicating that the critical effects of large-area MoS₂ monolayer substrates on the structural revolutions of MoS₂ monolayer sheets due to the weak interlayer van der Waals interactions between them. Figure 3d shows the values of R_g of substrate-hosted MoS₂ monolayer sheets as a function of MD relaxation time. Apparently, substrate-hosted MoS₂ monolayer sheets with high desulphurization contents show distinct developments and R_g values, which are different from those of free-standing MoS₂ sheets. These indicate that their different structural morphologies. These desulphurization-induced features of development of energetics and R_g can be similarly observed in other substrate-hosted MoS₂ sheets with planar dimensions of 20×20 - 50×50 nm² and length-to-width ratio of 2:1 to 5:1 (Figures S12-S15, and S17-S20).

As shown in Figures S1, S6, S11, and S16, the total energy of free-standing and substrate-hosted desulphurized MoS₂ monolayer sheets with different planar dimensions and ratios of length-to-width can converge to constant values, indicating that the relatively relaxed stable states of MoS₂ samples compared to their initial states. To understand the relatively relaxed stable states of MoS₂ samples, Figures 4 and 5 collect the average atomic potential energy per atom of both free-standing and substrate-hosted desulphurized MoS₂ monolayer sheets with different dimensions and ratios of length-to-width, respectively. The average atomic potential energy per atom in Figures 4 and 5 can be estimated from the instantaneous atomic potential energy during the MD relaxation time. As shown in Figure 4a, when the sample size changes from 10×10 - 50×50 nm², free-standing MoS₂ sheets with desulphurization contents

of 0-60% show slight reduction tendency in the average potential energy per Mo atom except for the desulphurization of 30%, whereas for that with desulphurization contents of 60-100%, the average potential energy per Mo atom is either slightly increased or nearly kept at an average constant value. Such transition behavior in the potential energy per Mo atom suggests that free-standing MoS₂ sheets with different dimensions shows different structural morphologies at critical desulphurization contents. With regard to free-standing MoS₂ sheets with different ratios of length-to-width, it is identified from Figure 4d that the average potential energy per Mo atom is monotonically slightly reduced with the increasing ratio of length-to-width, particularly for that with desulphurization content of 100%. For the case of bottom-S atom (Figures 4b and 4e), free-standing MoS₂ sheets with low desulphurization contents show reduction in the average potential energy per bottom-S atom with increasing dimension sizes and ratios of length-to-width. However, those with high desulphurization content show complex changes in average potential energy per bottom-S atom with increasing dimension sizes and ratios of length-to-width. Upon the case of top-S atom (Figures 4c and 4f), free-standing MoS₂ sheets show either reduction tendency or other complexed behaviors in the average potential energy per top-S atom with increasing dimension sizes and ratios of length-to-width, depending on the desulphurization contents. As seen in Figure 5a and d, all substrate-hosted desulphurized MoS₂ monolayer sheets with different dimensions and ratios of length-to-width show a reduction trend in the average atomic potential energy per Mo atom with increasing both sample size and ratios of length-to-width, and the reduction becomes less pronounced with increasing sample sizes and ratios of length-to-width. With regard to the case of surface bottom- and top-S atoms, however, there is a critical desulphurization content in the tendency change of the average atomic potential energy per bottom- or top-S atom. For example, below the desulphurization content of 30%, all MoS₂ samples show negligible reductions or increments in the average potential energy per bottom-S atom, whereas above which, they show obvious rising behaviors in the average potential energy per bottom-S atom, and then the rising behaviors become less significant with the increasements of sample dimensions and ratios of length-to-width (Figure 5b and e). For the case of top-S atoms, it is found that, above

desulphurization content of 30%, the average potential energy per top-S atom is monotonically increased with increasing sample dimensions and ratios of length-to-width, whereas below which, substrate-hosted MoS₂ samples show very slight changes in the average atomic potential energy per top-S atom. By comparison with free-standing MoS₂ sheets with substrate-hosted MoS₂ samples, for a given desulphurized MoS₂ sheet with a given dimension and a ratio of length-to-width, the average atomic potential energy per Mo- or S atom in substrate-hosted MoS₂ samples are always less than those in free-standing MoS₂ samples except for some cases with low desulphurization contents. This is mainly due to the fact that there are different interatomic interactions and vdW interactions between free-standing and substrate-hosted MoS₂ systems.

3.2 Desulphurization-induced Changes in Morphology of MoS₂ Sheets

Distinct energetics and radii of gyration in both free-standing and substrate-hosted MoS₂ monolayer sheets with different desulphurization contents suggest that their structural morphologies can be tuned by desulphurization. To provide more insights into desulphurization-induced change in morphology of monocrystalline MoS₂ monolayer sheets, the developments of structural morphology of MoS₂ samples are recorded during the structural relaxations. Figure 6 displays the snapshots of free-standing MoS₂ monolayer sheets with a planar dimension of $20 \times 20 \text{ nm}^2$ at desulphurization contents of 10%, 20%, 30%, 40%, 70% and 90% after relaxation times of 0 and 2 ns. To highlight desulphurization-induced wrinkling in free-standing MoS₂ sheets, atoms are rendered on the basis of relative displacements along out-of-plane (z) direction. Clearly, the structural morphology of free-standing MoS₂ sheets can be strongly affected by desulphurization. After structural optimization (zero MD relaxation time), there are large out-of-plane atomic displacements in the edges of free-standing MoS₂ monolayer sheets. After MD relaxation of 2 ns, however, their planar morphologies are remarkably changed. When the desulphurization content is below 30%, free-standing MoS₂ sheets wrinkles with low amplitude of out-of-plane fluctuations, and the out-of-plane displacement becomes more pronounced with increasing desulphurization contents, as shown in

Figures 6a-6f. As is known, intrinsic and dynamic wrinkling of MoS₂ change their optoelectronic and electromechanical properties, for example, coupled electronic and optical responses of MoS₂ can be altered by dynamic control of wrinkling degrees of freedom [56, 57](#). At desulphurization contents of 40-60%, free-standing MoS₂ monolayer sheets roll into a nanotube. Such interesting phenomenon was also detected from the previous experimental results [29](#). When the desulphurization content is about 70%, however, the edges in free-standing MoS₂ monolayer sheets show high ability of wrinkling, resulting in a hierarchy triangle structure with nanotube edges, as illustrated in Figure 6j. Once the desulphurization content exceeds 80%, a unique structure of diagonal-folding can form (Figure 6l).

Figure 7 shows the snapshots of substrate-hosted MoS₂ monolayer sheets with a planar dimension of $20 \times 20 \text{ nm}^2$ at desulphurization contents of 0%, 40%, 50%, 60%, 80% and 90% after relaxation times of 0 and 2 ns, where atoms are colored based on the relative atomic displacements along the out-of-plane (z) direction. Similarly, the desulphurization content plays a critical role in the structural morphology of substrate-hosted MoS₂ monolayer sheets. At low desulphurization contents of 0-20%, substrate-hosted MoS₂ monolayer sheets well stick to the substrate of MoS₂ monolayer as a result of vdW interactions between the substrate-hosted MoS₂ monolayer and the large-area MoS₂ monolayer substrate, resulting in a flat morphology of substrate-hosted MoS₂ monolayer sheets. As the desulphurization content reaches about 30-40%, quadrangular corners in substrate-hosted MoS₂ monolayer sheets are folded, forming localized wrinkling structures; whereas the interior bulk MoS₂ monolayer still sticks to the large-area MoS₂ monolayer substrate, remaining a flat morphology. Once the desulphurization content reaches around 50%, however, the substrate-hosted MoS₂ monolayer sheets are not able to remain flat morphology, but roll into structural morphology of a nanotube, similar to the case of free-standing MoS₂ sheets with a planar dimension of $20 \times 20 \text{ nm}^2$ at desulphurization contents of 40-60%. When the desulphurization content is 60%, the substrate-hosted MoS₂ monolayer sheets form a triangle wrinkled nanotube structure, analogous to the case of free-standing MoS₂ sheet with a planar dimension of $20 \times 20 \text{ nm}^2$ at the

desulphurization content of 70%. As the desulphurization content ranges from 70-80%, the substrate-hosted MoS₂ monolayer sheets roll into a closed diagonal-folding nanotube structure that shows non-uniform diameter along the wrinkling axis. Once the desulphurization content reaches 90%, the edges of substrate-hosted MoS₂ monolayer sheets promptly roll into small wrinkled nanotube structures, forming wrinkled quadrangle with nanotube edges. Obviously, the substrate-hosted MoS₂ monolayer sheets show more diverse structural morphologies via desulphurization than those of free-standing MoS₂ monolayer sheets.

3.3 Desulphurization-controlled Morphological Diagrams

Figure 8 summaries the morphological diagrams of free-standing desulphurized MoS₂ monolayer sheets with different planar dimensions and ratios of length-to-width, and here four distinct structural morphologies are defined as illustrated by the insets. As is seen from Figure 8a, the free-standing MoS₂ monolayer sheets with dimensions from 10 × 10 to 50 × 50 nm² show wrinkle morphology at low desulphurization contents, nanotube morphology at intermediate desulphurization contents, and diagonal-folding morphology at high desulphurization contents. Interestingly, a novel triangular-tube morphology can be only detected in free-standing MoS₂ monolayer sheets with dimensions of 20 × 20 - 40 × 40 nm² at intermediate desulphurization contents. The critical desulphurization content of changing structural morphology of free-standing MoS₂ monolayer sheets from one to another depends on the dimension sizes. As is shown in Figure 8b, all free-standing MoS₂ monolayer sheets with ratios of length-to-width from 2:1 to 5:1 primarily form wrinkle and nanotube morphology, which are also observed in MoS₂ sheets with dimensions of 10 × 10 - 50 × 50 nm². Moreover, only free-standing MoS₂ monolayer sheets with a length-to-width ratio of 1:1 exhibits the diagonal-folding structural morphology at high desulphurization contents. However, free-standing MoS₂ monolayer sheets with ratios of length-to-width of 2:1 - 5:1 are not able to show triangular-nanotube morphology through desulphurization, differing from that the case of square-shaped samples.

Figure 9 summarizes the morphological diagrams of substrate-hosted desulphurized MoS₂ monolayer sheets with different planar dimensions and ratios of length-to-width, and here seven distinct structural morphologies are illustrated by the insets for clarity. As displayed in Figure 9a, substrate-hosted MoS₂ monolayer sheets with planar dimensions of 10 × 10 - 50 × 50 nm² is able to show flat morphology at low desulphurization contents. With the increasing desulphurization contents, substrate-hosted MoS₂ monolayer sheets can form wrinkles, nanotube, diagonal-folding, or triangular-tube morphologies depending on the planar dimensions of substrate-hosted MoS₂ monolayer sheets. At high desulphurization contents, substrate-hosted MoS₂ monolayer sheets with a planar dimension of 10 × 10 nm² is structurally dissociated to form fracture amorphous cluster as the desulphurization content ranges from 70-100%. In contrast, substrate-hosted MoS₂ monolayer sheets with dimensions of 20 × 20 to 50 × 50 nm² is able to form quadrangle-tube morphology at high desulphurization contents. These diverse morphologies, *e.g.*, wrinkles, can be controlled by desulphurization contents. Previous studies showed that the desulphurization in MoS₂ sheets can also introduce in-plane strains to widen the wrinkles [24](#), [26](#), [58](#). It is noted that only substrate-hosted MoS₂ monolayer sheets with the dimension of 20 × 20 nm² is able to show nanotube morphology as the desulphurization content is 50%. As shown in Figure 9b, when the ratio of length-to-width is changed, substrate-hosted MoS₂ monolayer sheets show complex morphology diagrams similar to those of square-shaped MoS₂ samples. MoS₂ Samples with each ratio of length-to-width are able to show different distinct structural morphologies as the desulphurization content is increased from 0-100%. For example, substrate-hosted MoS₂ monolayer sheets with ratios of length-to-width of 2:1 - 5:1 show flat morphology at low desulphurization contents, but nanotube morphology at high desulphurization contents, differing from the case of square-shaped substrate-hosted MoS₂ monolayer sheets. It should be noted that substrate-hosted MoS₂ monolayer sheets with a length-to-width ratio of 1:1 show fracture amorphous nanocluster at high desulphurization contents.

The different structural morphology phases of desulphurized MoS₂ sheets as shown in Figures 8-9 indicate that the critical role of the weak interlayer van der Waals interactions on the structural morphology of desulphurized MoS₂. Critically, self-assembled structural behaviors of desulphurized MoS₂ monolayer sheets can be determined by S vacancies. On the one hand, followed by occurrence of the unique self-assembled behaviors, the stability and physical properties of MoS₂ can be adjusted with self-assembled new changed structural morphologies^{59, 60}. More specifically, the stability of MoS₂ is always on the dynamic changes, which is indicated by the dynamic development of energetics and radius of gyration of desulphurized MoS₂ monolayer sheets. On the other hand, the introduction of S vacancies is able to result in occurrence of planar strains, substrates, *e.g.*, large-area MoS₂ monolayer sheets, may serve as excellent templates to accommodate the planar strains in MoS₂ monolayer. Interestingly, as desulphurization contents is above the critical contents, the planar strains in MoS₂ monolayer sheets can not be accommodated by the substrates. Followed by this case, various complex structural morphologies of desulphurized MoS₂ monolayer sheets appear. In a nutshell, structural morphologies of free-standing and substrate-hosted MoS₂ monolayer sheets are strongly dependent on the desulphurization contents, planar dimensions and ratios of length-to-width. These suggest that structural morphologies of MoS₂ monolayer sheets with a given planar dimension can be finely tuned via desulphurization defect engineering.

4 Conclusions

In summary, classical MD simulations with a many-body reactive empirical bond order potential are performed to investigate the structural morphology of desulphurized MoS₂ monolayer sheets. Both instantaneous and average atomic potential energy per atom of MoS₂ monolayer sheets with different desulphurization contents, planar dimensions and ratios of length-to-width are recorded to elaborate the desulphurization-induced structural self-assembling behaviors. Self-assembled topological structures of both free-standing and substrate-hosted MoS₂ monolayer sheets driven by thermal fluctuations and interatomic interactions strongly depend on the desulphurization contents, planar dimensions and ratios

of length-to-width. Interestingly, it is demonstrated that the weak interlayer vdW interactions can also affect the structural morphology of desulphurized MoS₂ sheets. Similar to previous reports via experimental observations, MoS₂ monolayer sheets with specific conditions including desulphurization and sample dimensions can roll up into nanotube morphology. Besides, some other novel molecular structures, *e.g.*, triangular-tube, diagonal-folding, quadrangle-tube, and amorphous-cluster structures, are also observed, suggesting complex structural morphology phases of desulphurized MoS₂ monolayer sheets that are experimental pending. The study not only presents further knowledge of structural properties of 2D MoS₂ monolayer sheets, but also potentially provides new opportunities to synthesize TMD with unique morphologies via defect engineering.

ASSOCIATED CONTENT

Supporting Information

The Supporting Information is available free of charge at <https://xxx>.

AUTHOR INFORMATION

Corresponding Author

*pinqiang@wust.edu.cn; and jianyang@xmu.edu.cn;

Author contributions

J. W., and P. C. conceptualized and conceived the project. P. C. performed the molecular dynamics simulations and drew pictures with the important inputs and suggestions from the all co-authors. P. C., and J. W. analyzed and discussed the results. J. W., and P.C. wrote and polished the manuscript.

Acknowledgments

This work is financially supported by the National Natural Science Foundation of China (Grant Nos. 11772278 and 11904300), the Jiangxi Provincial Outstanding Young Talents Program (Grant No. 20192BCBL23029), the Fundamental Research Funds for the Central Universities (Xiamen University: Grant Nos. 20720180014 and 20720180018). Y. Yu and Z. Xu from Information and Network Center of Xiamen University for the help with the high-performance computer.

Competing interests

The authors declare that they have no competing interests.

Data and materials availability

All data needed to evaluate the conclusions in the paper are present in the paper and/or the Supplementary Materials. Additional data related to this paper may be requested from the corresponding authors.

References

1. M. Xu, T. Liang, M. Shi and H. Chen, *Chem. Rev.*, 2013, **113** (5), 3766-3798.
2. Q. H. Wang, K. Kalantar-Zadeh, A. Kis, J. N. Coleman and M. S. Strano, *Nature Nanotech*, 2012, **7** (11), 699-712.
3. J.-w. Seo, Y.-w. Jun, S.-w. Park, H. Nah, T. Moon, B. Park, J.-G. Kim, Y. J. Kim and J. Cheon, *Angew. Chem. Int. Ed.*, 2007, **46** (46), 8828-8831.
4. K. F. Mak, K. He, J. Shan and T. F. Heinz, *Nature Nanotech*, 2012, **7** (8), 494-498.
5. R. R. Chianelli, M. H. Siadati, M. P. De la Rosa, G. Berhault, J. P. Wilcoxon, R. Bearden and B. L. Abrams, *Catal. Rev.*, 2006, **48** (1), 1-41.
6. M. Chhowalla, H. S. Shin, G. Eda, L.-J. Li, K. P. Loh and H. Zhang, *Nature Chem*, 2013, **5** (4), 263-275.
7. A. Kuc and T. Heine, *Chem. Soc. Rev.*, 2015, **44** (9), 2603-2614.
8. G. Eda, H. Yamaguchi, D. Voiry, T. Fujita, M. Chen and M. Chhowalla, *Nano Lett.*, 2011, **11** (12), 5111-5116.
9. K. F. Mak, C. Lee, J. Hone, J. Shan and T. F. Heinz, *Phys. Rev. Lett.*, 2010, **105** (13), 136805.
10. B. Radisavljevic, A. Radenovic, J. Brivio, V. Giacometti and A. Kis, *Nature Nanotech*, 2011, **6** (3), 147.
11. G. Eda, T. Fujita, H. Yamaguchi, D. Voiry, M. Chen and M. Chhowalla, *ACS Nano*, 2012, **6** (8), 7311-7317.
12. A. Splendiani, L. Sun, Y. Zhang, T. Li, J. Kim, C.-Y. Chim, G. Galli and F. Wang, *Nano Lett.*, 2010, **10** (4), 1271-1275.
13. K. Kam and B. Parkinson, *J. Phys. Chem.*, 1982, **86** (4), 463-467.
14. T. Li, *Phys. Rev. B*, 2012, **85** (23), 235407.
15. S. Bertolazzi, J. Brivio and A. Kis, *ACS Nano*, 2011, **5** (12), 9703-9709.
16. A. Castellanos-Gomez, M. Poot, G. A. Steele, H. S. J. van der Zant, N. Agrait and G. Rubio-Bollinger, *Adv. Mater.*, 2012, **24** (6), 772-775.
17. W. Wang, L. Li, C. Yang, R. Solercespo, Z. Meng, M. L. Li, X. Zhang, S. Keten and H. Espinosa, *Nanotechnology*, 2017, **28** (16), 164005.
18. J. Wu, G. Nie, J. Xu, J. He, Q. Xu and Z. Zhang, *Phys. Chem. Chem. Phys.*, 2015, **17** (48), 32425-32435.
19. Y. Yin, P. Miao, Y. Zhang, J. Han, X. Zhang, Y. Gong, L. Gu, C. Xu, T. Yao, P. Xu, Y. Wang, B. Song and S. Jin, *Adv. Funct. Mater.*, 2017, **27** (16), 1606694.
20. Y.-C. Lin, D. O. Dumcenco, Y.-S. Huang and K. Suenaga, *Nature Nanotech*, 2014, **9** (5), 391-396.

21. J. Zhao, L. Kou, J. W. Jiang and T. Rabczuk, *Nanotechnology*, 2014, **25** (29), 295701.
22. L. Hromadová, R. Martoňák and E. Tosatti, *Phys. Rev. B*, 2013, **87** (14), 144105.
23. K. Q. Dang, J. P. Simpson and D. E. Spearot, *Scripta Mater.*, 2014, **76**, 41-44.
24. W. Zhou, X. Zou, S. Najmaei, Z. Liu, Y. Shi, J. Kong, J. Lou, P. M. Ajayan, B. I. Yakobson and J.-C. Idrobo, *Nano Lett.*, 2013, **13** (6), 2615-2622.
25. Y. Chen, S. Huang, X. Ji, K. Adepalli, K. Yin, X. Ling, X. Wang, J. Xue, M. Dresselhaus, J. Kong and B. Yildiz, *ACS Nano*, 2018, **12** (3), 2569-2579.
26. J. Wu, P. Cao, Z. Zhang, F. Ning, S.-s. Zheng, J. He and Z. Zhang, *Nano Lett.*, 2018, **18** (2), 1543-1552.
27. J. Wu, H. Gong, Z. Zhang, J. He, P. Ariza, M. Ortiz and Z. Zhang, *Appl. Mater. Today*, 2019, **15**, 34-42.
28. H.-P. Komsa, J. Kotakoski, S. Kurasch, O. Lehtinen, U. Kaiser and A. V. Krashenninnikov, *Phys. Rev. Lett.*, 2012, **109** (3), 035503.
29. J. Meng, G. Wang, X. Li, X. Lu, J. Zhang, H. Yu, W. Chen, L. Du, M. Liao, J. Zhao, P. Chen, J. Zhu, X. Bai, D. Shi and G. Zhang, *Small*, 2016, **12** (28), 3770-3774.
30. Q. Ding, K. J. Czech, Y. Zhao, J. Zhai, R. J. Hamers, J. C. Wright and S. Jin, *ACS Appl. Mater. Interfaces*, 2017, **9** (14), 12734-12742.
31. H. Li, C. Tsai, A. L. Koh, L. Cai, A. W. Contryman, A. H. Fragapane, J. Zhao, H. S. Han, H. C. Manoharan, F. Abild-Pedersen, J. K. Nørskov and X. Zheng, *Nat. Mater.*, 2016, **15** (1), 48-53.
32. Y. Yin, J. Han, Y. Zhang, X. Zhang, P. Xu, Q. Yuan, L. Samad, X. Wang, Y. Wang, Z. Zhang, P. Zhang, X. Cao, B. Song and S. Jin, *J. Am. Chem. Soc.*, 2016, **138** (25), 7965-7972.
33. G. Li, D. Zhang, Q. Qiao, Y. Yu, D. Peterson, A. Zafar, R. Kumar, S. Curtarolo, F. Hunte, S. Shannon, Y. Zhu, W. Yang and L. Cao, *J. Am. Chem. Soc.*, 2016, **138** (51), 16632-16638.
34. H. Li, M. Du, M. J. Mleczko, A. L. Koh, Y. Nishi, E. Pop, A. J. Bard and X. Zheng, *J. Am. Chem. Soc.*, 2016, **138** (15), 5123-5129.
35. S. W. Han, Y. H. Hwang, S.-H. Kim, W. S. Yun, J. D. Lee, M. G. Park, S. Ryu, J. S. Park, D.-H. Yoo, S.-P. Yoon, S. C. Hong, K. S. Kim and Y. S. Park, *Phys. Rev. Lett.*, 2013, **110** (24), 247201.
36. M. C. Wang, J. Leem, P. Kang, J. Choi, P. Knapp, K. Yong and S. Nam, *2D Materials*, 2017, **4** (2), 022002.
37. D. Vella, J. Bico, A. Boudaoud, B. Roman and P. M. Reis, *Proc. Natl. Acad. Sci.*, 2009, **106** (27), 10901.
38. A. Castellanos-Gomez, R. Roldán, E. Cappelluti, M. Buscema, F. Guinea, H. S. J. van der Zant and G. A. Steele, *Nano Lett.*, 2013, **13** (11), 5361-5366.

39. J. W. Jiang, *Nanotechnology*, 2014, **25** (35), 355402.
40. Y. Guo and W. Guo, *J. Phys. Chem. C*, 2013, **117** (1), 692-696.
41. P. Cao, J. Wu, Z. Zhang and F. Ning, *Nanotechnology*, 2017, **28** (4), 045702.
42. K. Zhang and M. Arroyo, *J. Mech. Phys. Solids*, 2014, **72**, 61-74.
43. T. Liang, S. R. Phillpot and S. B. Sinnott, *Phys. Rev. B*, 2009, **79** (24), 245110.
44. T. Liang, S. R. Phillpot and S. B. Sinnott, *Phys. Rev. B*, 2012, **85** (19), 199903.
45. W. B. Donald, A. S. Olga, A. H. Judith, J. S. Steven, N. Boris and B. S. Susan, *J. Phys.: Condens. Matter*, 2002, **14** (4), 783.
46. W. Xiaonan, T. Alireza and E. S. Douglas, *Nanotechnology*, 2015, **26** (17), 175703.
47. D. M. Tang, D. G. Kvashnin, S. Najmaei, Y. Bando, K. Kimoto, P. Koskinen, P. M. Ajayan, B. I. Yakobson, P. B. Sorokin and J. Lou, *Nat. Commun.*, 2014, **5** (4), 3631.
48. E. W. Bucholz and S. B. Sinnott, *J. Appl. Phys.*, 2013, **114** (3), 791.
49. S. Xiong and G. Cao, *Nanotechnology*, 2015, **26** (18), 185705.
50. S. K. Singh, M. Neek-Amal, S. Costamagna and F. M. Peeters, *Phys. Rev. B*, 2015, **91** (1), 014101.
51. J. A. Stewart and D. E. Spearot, *Modell. Simul. Mater. Sci. Eng.*, 2013, **21** (4), 045003.
52. K. Q. Dang and D. E. Spearot, *J. Appl. Phys.*, 2014, **116** (1), 013508.
53. J. Wu, J. He, P. Ariza, M. Ortiz and Z. Zhang, *Int. J. Fract*, 2020, **223** (1), 39-52.
54. B. Wang, Z. Islam, K. Zhang, K. Wang, J. Robinson and A. Haque, *Nanotechnology*, 2017, **28** (36), 365703.
55. S. Plimpton, *J. Comput. Phys.*, 1995, **117** (1), 1-19.
56. E. M. Mannebach, R. Li, K.-A. Duerloo, C. Nyby, P. Zalden, T. Vecchione, F. Ernst, A. H. Reid, T. Chase, X. Shen, S. Weathersby, C. Hast, R. Hettel, R. Coffee, N. Hartmann, A. R. Fry, Y. Yu, L. Cao, T. F. Heinz, E. J. Reed, H. A. Dürr, X. Wang and A. M. Lindenberg, *Nano Lett.*, 2015, **15** (10), 6889-6895.
57. A. P. M. Barboza, H. Chacham, C. K. Oliveira, T. F. D. Fernandes, E. H. M. Ferreira, B. S. Archanjo, R. J. C. Batista, A. B. de Oliveira and B. R. A. Neves, *Nano Lett.*, 2012, **12** (5), 2313-2317.
58. A. Azizi, X. Zou, P. Ercius, Z. Zhang, A. L. Elías, N. Perealópez, G. Stone, M. Terrones, B. I. Yakobson and N. Alem, *Nat. Commun.*, 2014, **5**, 4867.
59. Y. Han, T. Hu, R. Li, J. Zhou and J. Dong, *Phys. Chem. Chem. Phys.*, 2015, **17** (5), 3813-3819.

60. H.-P. Komsa, S. Kurasch, O. Lehtinen, U. Kaiser and A. V. Krasheninnikov, *Phys. Rev. B*, 2013, **88** (3), 035301.

Figures and Tables

Figure 1

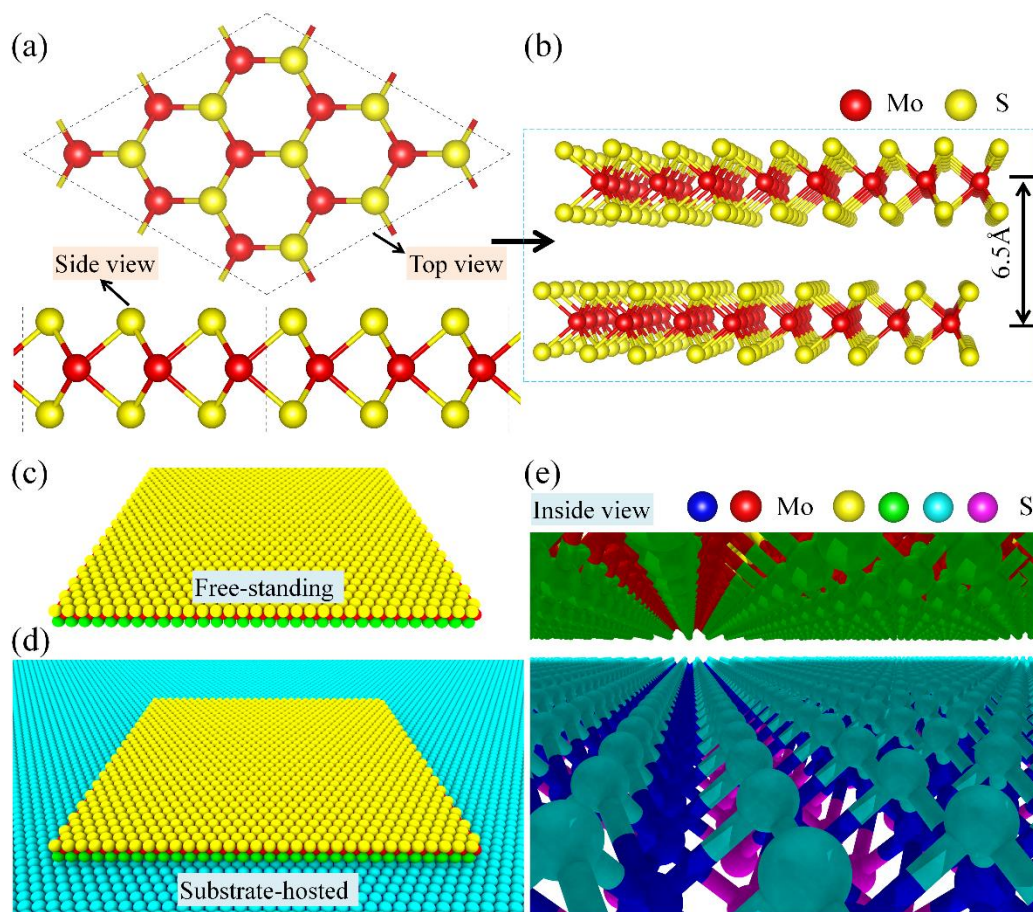


Figure 1 Atom structures of 2D monocrystalline MoS₂ sheets. (a) Top and side views of MoS₂ monolayer structures. (b) Representative structure of MoS₂ bilayer. (c) A free-standing molecular structure of MoS₂ monolayer sheet with a planar dimension of 10 × 10 nm². (d) A substrate-hosted molecular structure MoS₂ with a planar dimension of 10 × 10 nm². (e) A zoomed-in structure of substrate-hosted MoS₂ sheets at the initial state from the inside view.

Figure 2

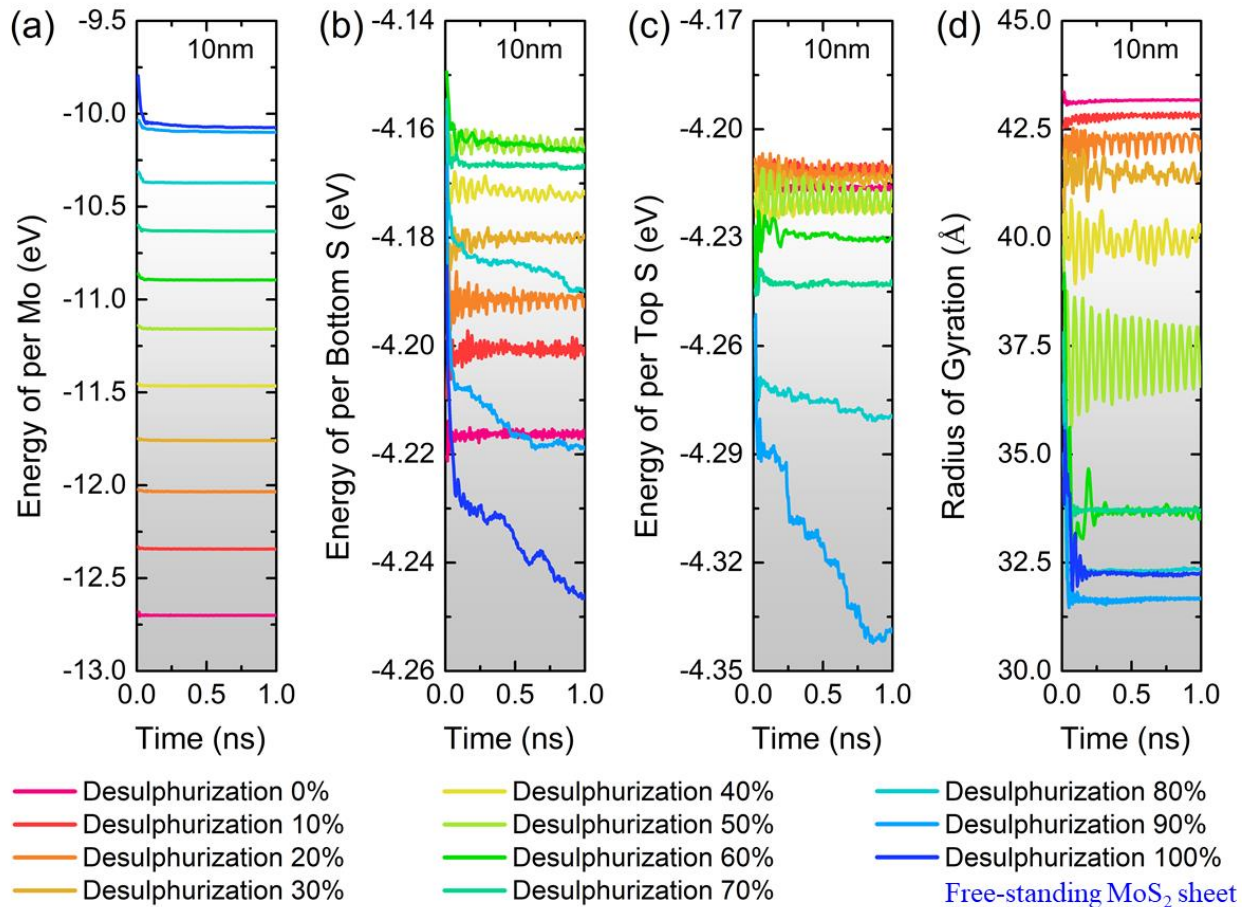


Figure 2 Energetics in free-standing MoS_2 monolayer sheets with a planar dimension of $10 \times 10 \text{ nm}^2$ and desulphurization ranging from 0 to 100%. (a) Relationships between energetics per Mo atom and relaxation time. (b) Relationships between energetics per bottom-S atom and relaxation time. (c) Relationships between energetics per top-S atom and relaxation time. (d) Relationships between radius of gyration and relaxation time.

Figure 3

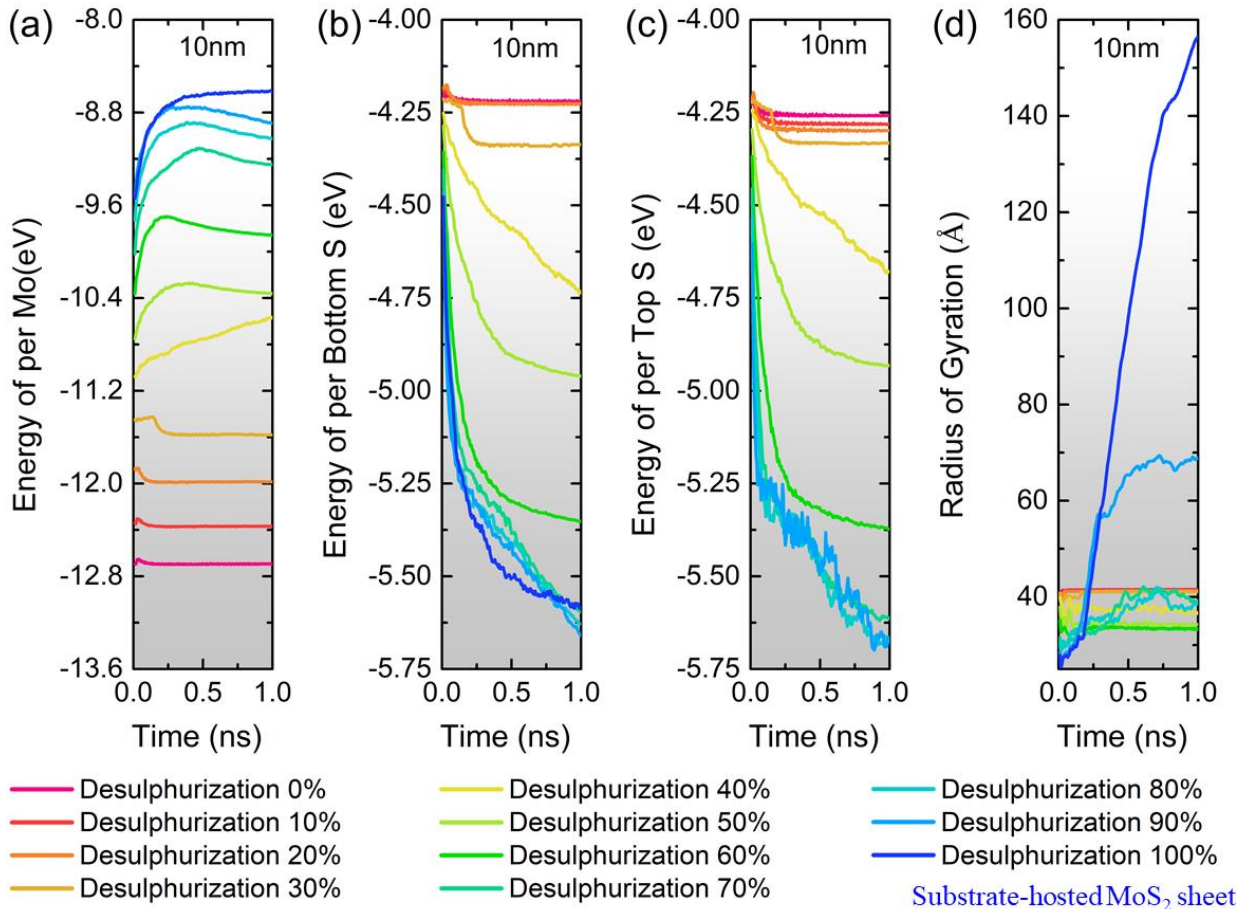


Figure 3 Energetics in substrate-hosted MoS₂ monolayer sheets with a planar dimension of 10 × 10 nm² and desulphurization ranging from 0 to 100%. (a) Relationships between energetics per Mo atom and relaxation time. (b) Relationships between energetics per bottom-S atom and relaxation time. (c) Relationships between energetics per top-S atom and relaxation time. (d) Relationships between radius of gyration and relaxation time.

Figure 4

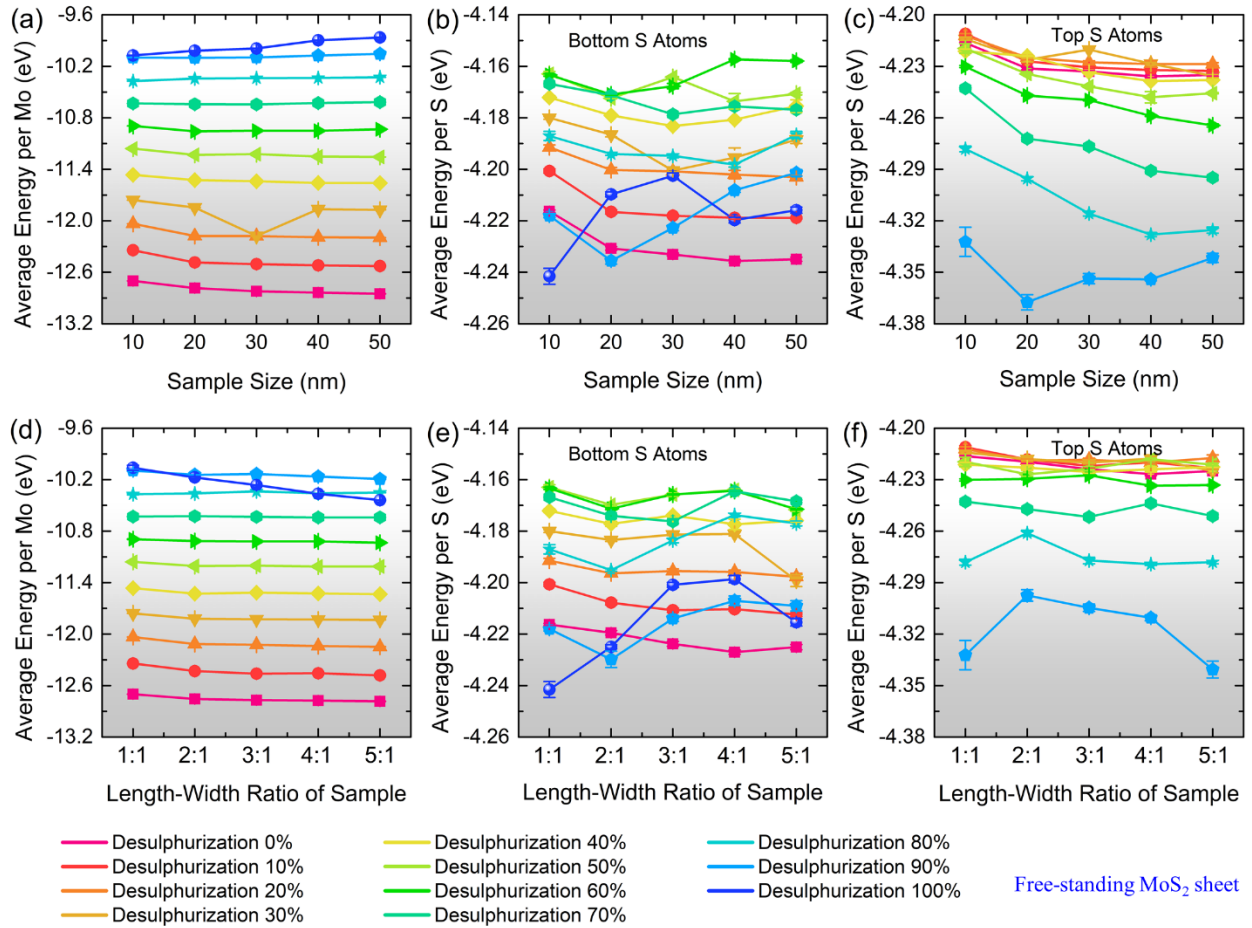


Figure 4 Average energy-per-atom of free-standing MoS₂ monolayer sheets. (a)-(c) Average energy-per-atom versus sample sizes. (d)-(f) Average energy-per-atom versus length-width ratios of samples.

Figure 5

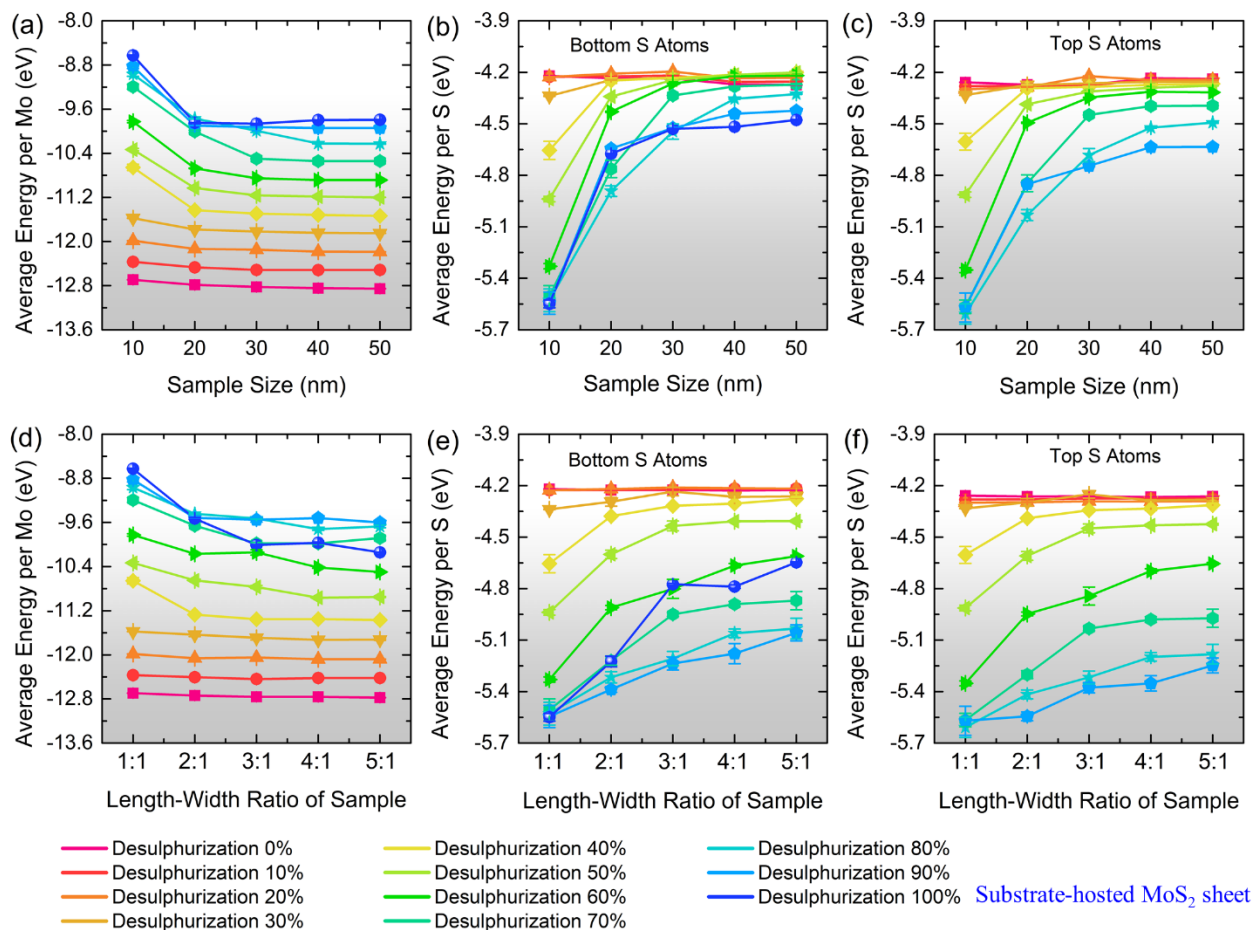


Figure 5 Average energy-per-atom of substrate-hosted MoS₂ monolayer sheets. (a)-(c) Average energy-per-atom versus sample sizes. (d)-(f) Average energy-per-atom versus length-width ratios of sample.

Figure 6

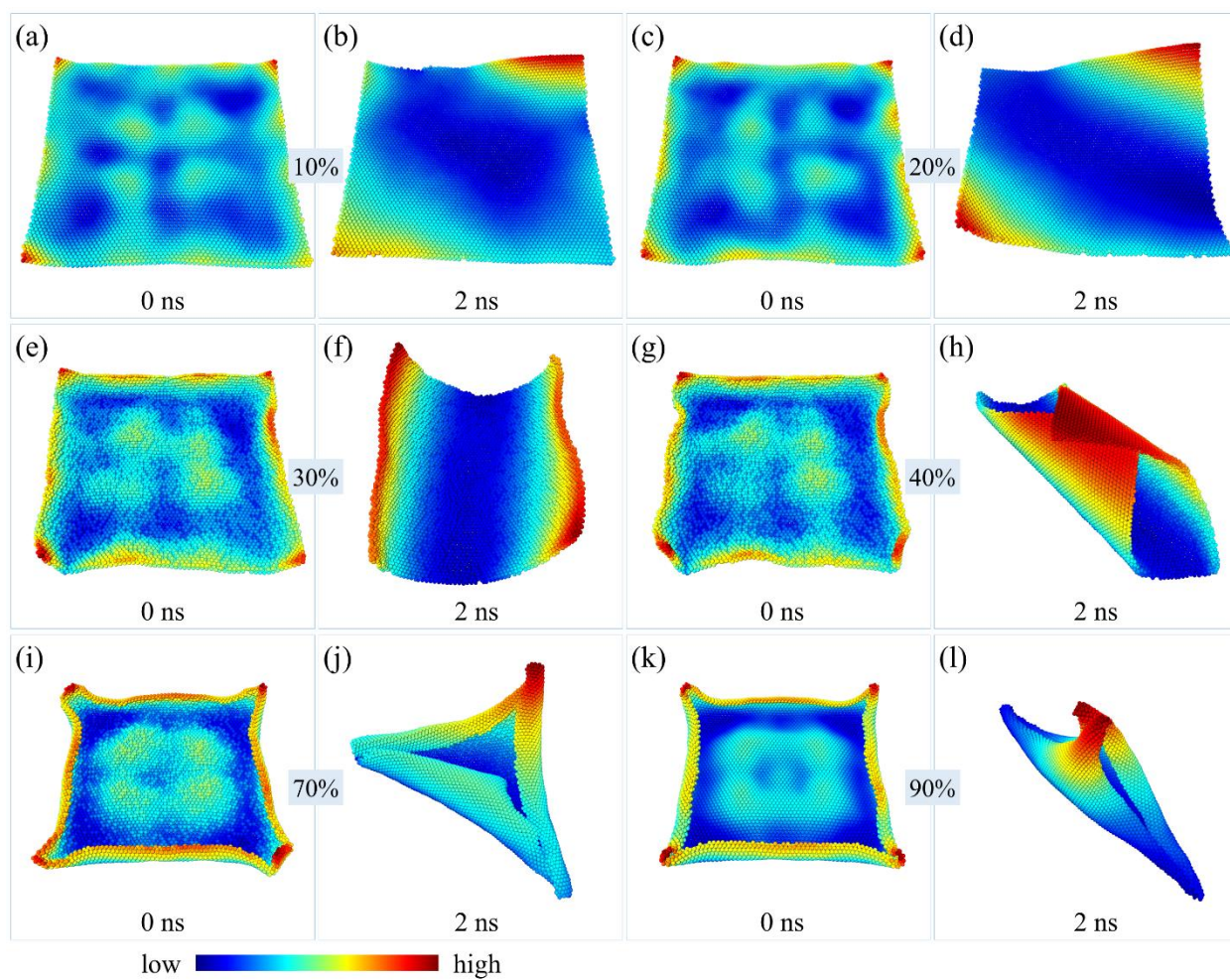


Figure 6 Structural revolutions of free-standing MoS₂ monolayer sheets with a planar dimension of 20 × 20 nm². Snapshots of free-standing MoS₂ monolayer sheets are colored on the basis of the relative displacements in out-of-plane (z) direction.

Figure 7

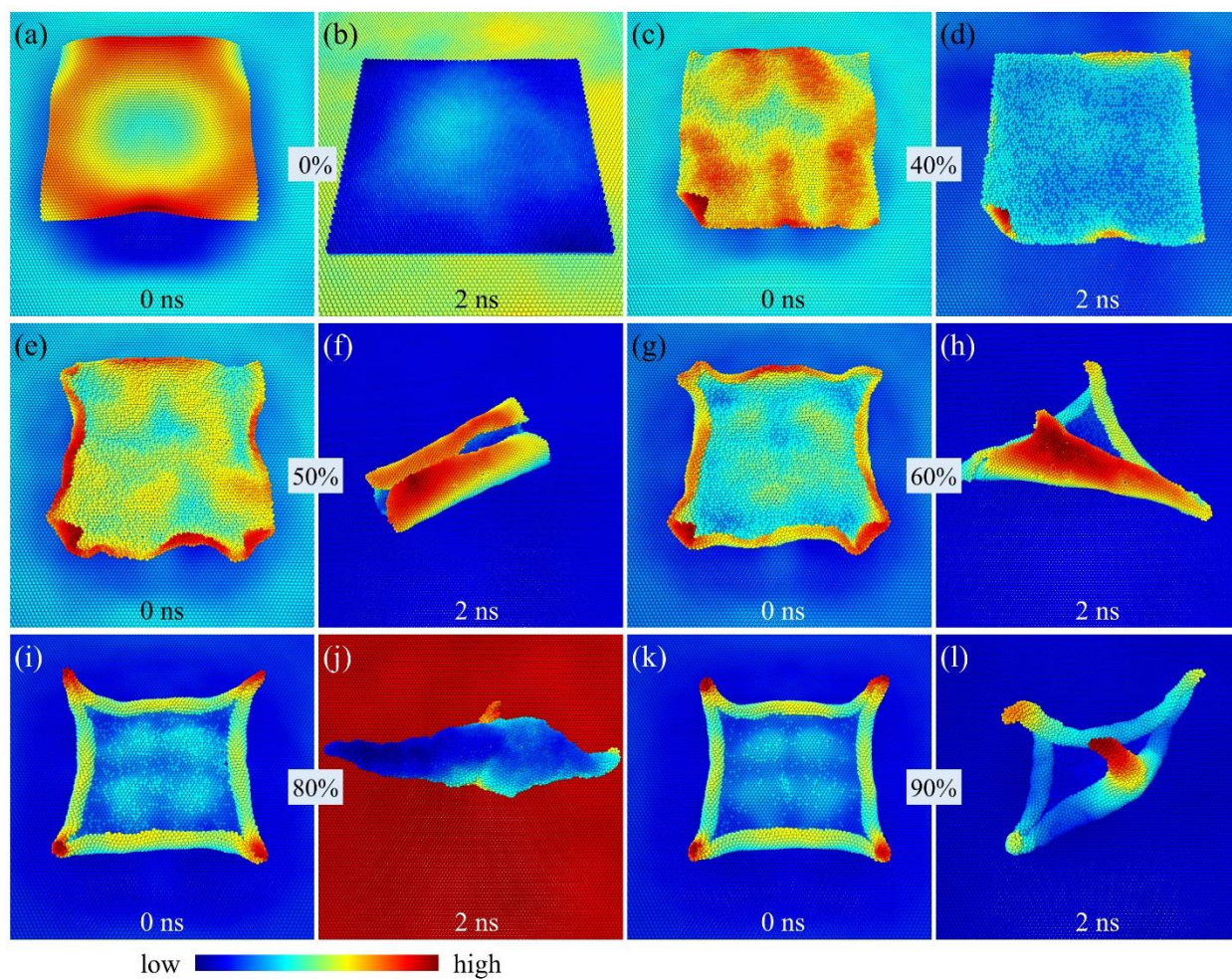


Figure 7 Structural revolutions of substrate-hosted MoS₂ monolayer sheets with a planar dimension of 20 × 20 nm². Snapshots of substrate-hosted MoS₂ monolayer sheets are colored according to the relative displacements in out-of-plane (*z*) direction.

Figure 8

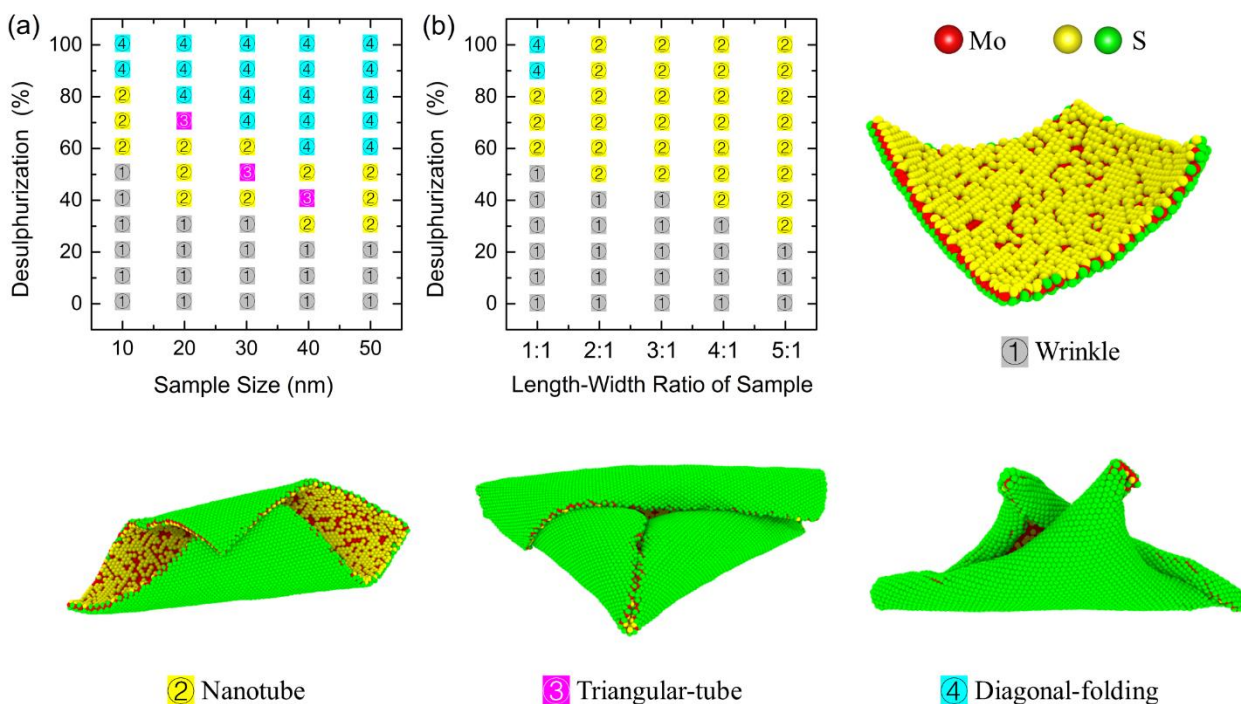


Figure 8 Molecular morphological diagrams of free-standing MoS_2 monolayer sheets. (a) Desulphurization versus sample size diagrams. (b) Desulphurization versus ratios of length-to-width diagrams. ① Relaxed molecular structure with a dimension $10 \times 10 \text{ nm}^2$ and desulphurization of 30%. ② Relaxed molecular structure with a dimension of $20 \times 20 \text{ nm}^2$ and desulphurization of 40%. ③ Relaxed molecular structure with a dimension of $30 \times 30 \text{ nm}^2$ and desulphurization of 50%. ④ Relaxed molecular structure with a dimension of $20 \times 20 \text{ nm}^2$ and desulphurization of 80%.

Figure 9

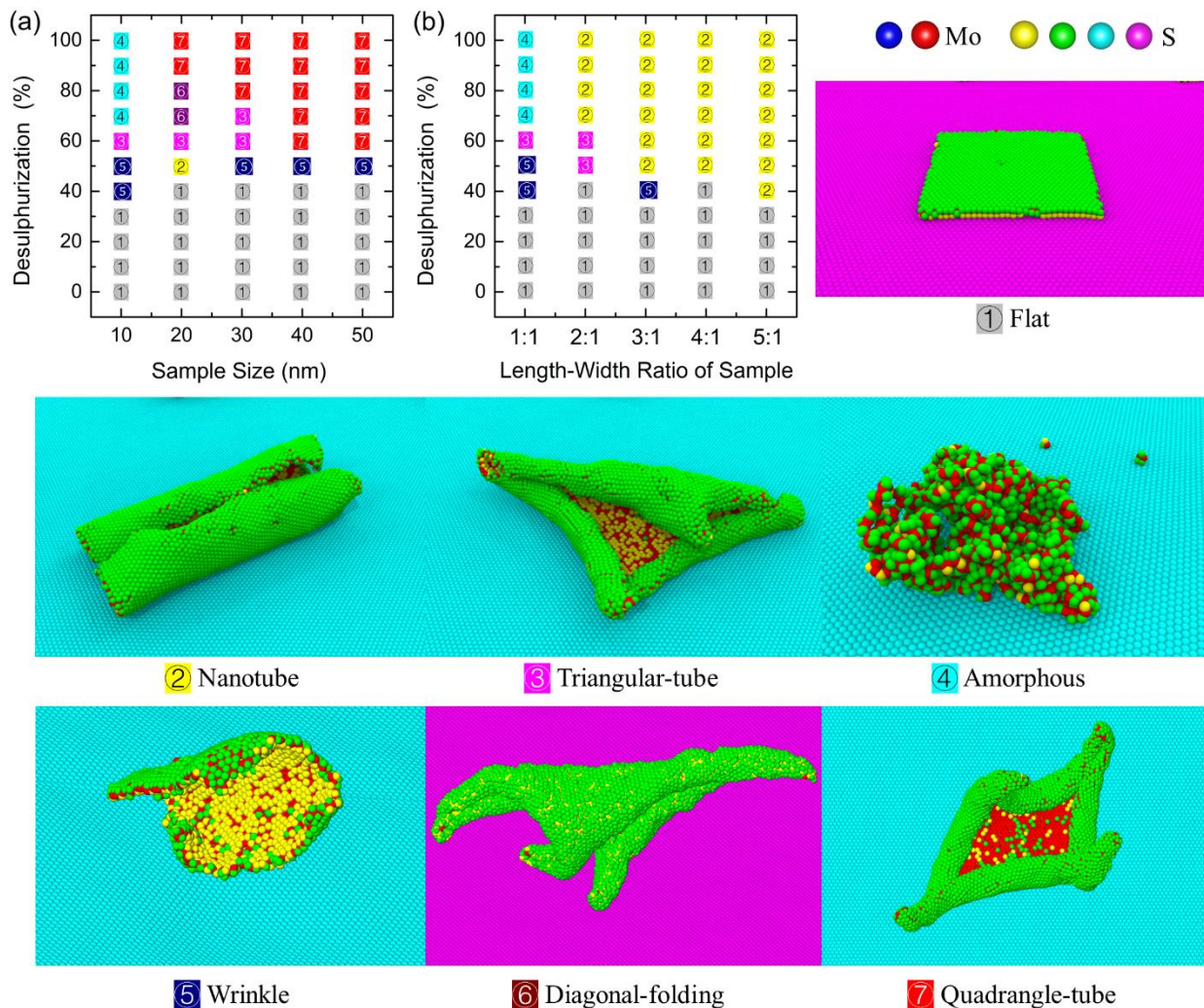


Figure 9 Molecular morphological diagrams of substrate-hosted MoS₂ monolayer sheets. (a) Desulphurization versus sample size diagrams. (b) Desulphurization versus ratios of length-to-width diagrams. ① Relaxed molecular structure with a dimension of 10 × 10 nm² and desulphurization of 20%. ② Relaxed molecular structure with a dimension of 20 × 20 nm² and desulphurization of 50%. ③ Relaxed molecular structure with a dimension of 20 × 20 nm² and desulphurization of 60%. ④ Relaxed molecular structure with a dimension of 10 × 10 nm² and desulphurization of 90%. ⑤ Relaxed molecular structure with a dimension of 10 × 10 nm² and desulphurization of 40%. ⑥ Relaxed molecular structure

with a dimension of $20 \times 20 \text{ nm}^2$ and desulphurization of 80%. ⑦ Relaxed molecular structure with a dimension of $20 \times 20 \text{ nm}^2$ and desulphurization of 90%.